

# Mechanical behaviour of granular materials used in analogue modelling: insights from grain characterisation, ring-shear tests and analogue experiments

Marion Panien, Guido Schreurs\*, Adrian Pfiffner

*Institute of Geological Sciences, University of Bern, Baltzerstrasse 1-3, CH-3012 Bern, Switzerland*

Received 15 November 2004; received in revised form 11 April 2006; accepted 10 May 2006

Available online 24 July 2006

## Abstract

The mechanical behaviour of several dry granular materials is investigated through ring-shear tests, grain characterisation, and simple analogue experiments analysed by X-ray computed tomography. An improved knowledge of granular materials is essential to determine their suitability as analogues for upper crustal rocks in experimental models and to compare analogue and numerical experiments.

The ring-shear tests show that the granular materials have an elastic/frictional plastic behaviour with strain-hardening preceding failure at peak strength, followed by strain softening until a dynamic-stable value is reached. This is similar to the behaviour exhibited by experimentally deformed rocks.

The physical characteristics of the grains determine the amount of diffuse deformation before failure, the percentage of strain softening and act on the thickness of the shear zones before broadening.

Initial shear zone width in extensional and contractional experiments is between 11 and 16 times the mean grain size. The angle of internal friction defining one of the mechanical properties of granular materials and thus fault dip is not only related to physical characteristics of the grains and to the handling technique used (e.g. sieving or pouring), but also to the overburden and to the experimental setup used.

© 2006 Elsevier Ltd. All rights reserved.

*Keywords:* Granular materials; Analogue modelling

## 1. Introduction

Analogue modelling has been used since the nineteenth century to simulate different kinds of natural geological structures in order to understand mechanisms controlling their geometry and kinematics. To simulate brittle deformation in the upper crust, dry granular materials are generally used. Natural quartz sand is the most commonly used granular material in analogue experiments at natural gravity conditions and its mechanical properties such as cohesion and coefficient of internal friction have been investigated by e.g. Hubbert (1951); Krantz

(1991a,b); Cobbold and Castro (1999); Schellart (2000) and Lohrmann et al. (2003). Other granular materials whose properties have been studied include glass microspheres (Krantz, 1991a,b; Schellart, 2000), aluminium hydroxide and siliceous microspheres (Rossi and Storti, 2003). The values of the scaled cohesion and the coefficient of internal friction obtained in these studies are generally comparable to those determined experimentally for upper crustal rocks by Byerlee (1978). Krantz (1991b); Schellart (2000) and Lohrmann et al. (2003) demonstrate that the coefficient of internal friction of granular materials depends on the physical handling technique (e.g. sifting or pouring) used to deposit the granular material in the shear test machine. Values of the scaled cohesion and of the coefficient of internal friction are also influenced by the shape of the grains (Schellart, 2000). Grain size and grain size distribution, however, seem to have no or

\* Corresponding author.

*E-mail address:* schreurs@geo.unibe.ch (G. Schreurs).

little effect on these values according to Schellart (2000) and Lohrmann et al. (2003).

Analogue modellers have generally assumed that quartz sand and other granular materials deform according to the Coulomb failure criterion with constant frictional properties. However, granular materials display a more complex behaviour (e.g. Schanz and Vermeer, 1996). Lohrmann et al. (2003) show that quartz sand does not have constant frictional properties but is characterised by elastic/frictional plastic behaviour with strain-hardening preceding failure and subsequent strain-softening until a stable value is reached. However, such a mechanical behaviour for quartz sand is very similar to the one exhibited by experimentally deformed rocks (Mandl, 1988; Marone, 1998; Barnhoorn et al., 2004).

In this study we analyse different natural and artificial granular materials in order to test their suitability for simulating upper crustal rocks in analogue modelling experiments at natural gravity conditions. We also aim to improve our knowledge of the mechanical behaviour of granular materials, which is essential for scaling models as correctly as possible (Hubbert, 1937; Ramberg, 1981) and for comparing analogue and numerical experiments (Ellis et al., 2004). First, we determine physical characteristics such as density, grain size distribution and grain shape. In addition, we measure the X-ray attenuation of the granular materials, which is of importance when X-ray computed tomography (CT) is used to analyse analogue models (e.g. Colletta et al., 1991; Schreurs et al., 2001). In a second step, we determine the cohesion and friction coefficients of the materials using a ring-shear tester and examine fault inception in simple analogue experiments analysed by X-ray CT. Subsequently, the physical characteristics and results from the analogue experiments are used to interpret the measured mechanical properties of the granular materials.

## 2. Physical characteristics

Besides quartz sand that is commonly used to simulate brittle deformation in analogue model experiments, five other granular materials are examined: brown corundum, white corundum, glass fragments, Pyrex and glass microbeads. The quartz sand is a natural Triassic sand from Schnaittenbach (Germany) whereas all the other granular materials are artificial products. Brown and white corundum are derived from bauxite and pure clay, respectively. Microbeads, Pyrex and glass fragments are all glass products. Microbeads are high-quality vaporised glass spheres made by Worf Glaskugeln

company in Mainz (Germany), Pyrex is a grinded borosilicate glass and glass fragments are from crushed recycled glass products. Glass fragments, quartz sand, microbeads, white and brown corundum are abrasive particles usually used for sandblasting. The chemical composition of the materials that have been investigated and some of their physical properties are listed in Tables 1 and 2.

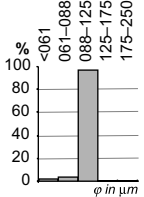
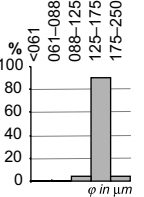
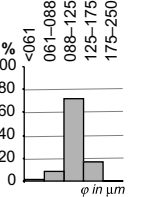
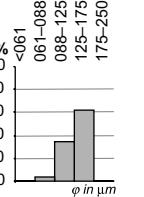
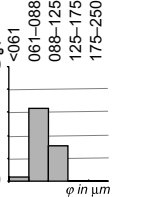
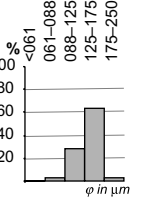
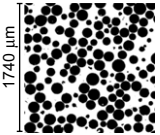
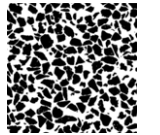
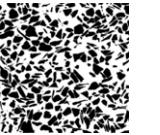

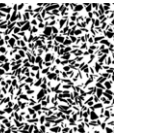
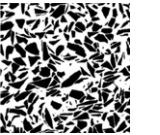
Although the range of the grain size is given by the suppliers, we determine the grain size distribution of the different materials using sieves with different mesh sizes. Grain size distribution is expressed in terms of weight percent between two sieve fractions and shown in the histograms of Table 2. Both quartz sand and microbeads have 90% of the grains falling within one fraction (125–175  $\mu\text{m}$  for quartz sand and 88–125  $\mu\text{m}$  for microbeads). The other granular materials display a more heterogeneous grain size distribution: brown corundum has 70% of the grains falling between 80 and 125  $\mu\text{m}$ , whereas white corundum and glass fragment each have 60% between 125 and 175  $\mu\text{m}$ , and Pyrex has 60% between 61 and 88  $\mu\text{m}$ .

Grain density has been determined using a pycnometer and the values for the different granular materials are listed in Table 2, with Pyrex having the lowest density (2.26  $\text{g}/\text{cm}^3$ ) and brown and white corundum the highest density with values slightly above 4  $\text{g}/\text{cm}^3$ . Contrary to grain density, bulk density takes both grains size and porosity into account. The bulk density has been determined by measuring the mass of a known volume of a material with an electronic balance. Measurements have been done not only for different granular materials, but also for the same material using two different physical handling techniques that consist of either rapid pouring at once from a height of ca. 10 cm into a recipient or sifting from a height of about 30 cm with a filling rate of ca. 200  $\text{cm}^3/\text{minute}$ . Repeated measurements were made for each material and technique, and averaged (Table 2). The results show that bulk density depends both on the material and on the handling technique. As shown previously by Krantz (1991a,b) and Lohrmann et al. (2003), the density of poured materials is lower than that of sifted materials. Sifting of granular materials generates more densely packed sands, whereas rapid pouring produces under-compacted sands. Density values of Pyrex and microbeads show little dependence on the handling technique used. Differences between poured and sifted values are smallest for microbeads (5.4%) and largest for glass fragments (19%). The same holds for the porosity values, which vary inverse proportionally to density values (Table 2).

Table 1  
Chemical composition of the tested materials

Quartz sand		Brown corundum		White corundum		Glass fragments		Pyrex		Microbeads	
SiO <sub>2</sub>	99%	Al <sub>2</sub> O <sub>3</sub>	95.2–95.8%	Al <sub>2</sub> O <sub>3</sub>	99.5–99.8%	SiO <sub>2</sub>	72.5%	SiO <sub>2</sub>	80.6%	SiO <sub>2</sub>	72.5%
Al <sub>2</sub> O <sub>3</sub>	0.4%	SiO <sub>2</sub>	0.5–0.8%	SiO <sub>2</sub>	0.1%	Na <sub>2</sub> O	13.7%	B <sub>2</sub> O <sub>3</sub>	13.0%	Na <sub>2</sub> O	13.8%
Fe <sub>2</sub> O <sub>3</sub> + TiO <sub>2</sub>	0.05%	TiO <sub>2</sub>	2.6%	FeO	<0.03%	CaO	9.8%	Na <sub>2</sub> O	4.0%	CaO	8.2%
CaO + MgO	0.05%	Fe <sub>2</sub> O <sub>3</sub>	<0.2%	TiO <sub>2</sub>	0.01%	MgO	3.3%	Al <sub>2</sub> O <sub>3</sub>	2.3%	MgO	3.7%
K <sub>2</sub> O/Na <sub>2</sub> O	0.2%	CaO/MgO	<0.9%	Na <sub>2</sub> O	0.1%	Al <sub>2</sub> O <sub>3</sub>	0.4%			Al <sub>2</sub> O <sub>3</sub>	1.4%
Glühverlust	0.2%	Free Fe	<0.1%	Free Fe	0%						

Table 2  
Physical characteristics of tested granular materials. Images are obtained with a binocular microscope. Grain shape is expressed by texture, roundness, form and SHI and PARIS shape factors

	microbeads	quartz sand	brown corundum	white corundum	Pyrex	glass fragments
<b>origin</b>	high-quality vaporised glass	Triassic quartz sand	bauxite	pure clay	borosilicate	recycled glass products
<b>main chemical component</b>	72.5 % SiO <sub>2</sub>	99 % SiO <sub>2</sub>	95 % Al <sub>2</sub> O <sub>3</sub>	99 % Al <sub>2</sub> O <sub>3</sub>	SiO <sub>2</sub>	72.5 % SiO <sub>2</sub>
<b>average attenuation value</b>	951 HU	874 HU	1244 HU	1073 HU	355 HU	688 HU
<b>grain size range</b> (as indicated by supplier)	70–110 μm	80–200 μm	88–125 μm	105–149 μm	100 μm	100–210 μm
<b>grain size distribution</b>						
<b>grain density</b>	2.5 g/cm <sup>3</sup>	2.68 g/cm <sup>3</sup>	4.05 g/cm <sup>3</sup>	4.09 g/cm <sup>3</sup>	2.26 g/cm <sup>3</sup>	2.54 g/cm <sup>3</sup>
<b>bulk density:</b>						
sifted	1.48 g/cm <sup>3</sup>	1.56 g/cm <sup>3</sup>	1.89 g/cm <sup>3</sup>	1.89 g/cm <sup>3</sup>	1.09 g/cm <sup>3</sup>	1.24 g/cm <sup>3</sup>
poured	1.4 g/cm <sup>3</sup>	1.32 g/cm <sup>3</sup>	1.55 g/cm <sup>3</sup>	1.57 g/cm <sup>3</sup>	0.97 g/cm <sup>3</sup>	1 g/cm <sup>3</sup>
<b>porosity:</b>						
sifted	29.6 %	28.8 %	34.4 %	33.7 %	33.3 %	34.6 %
poured	30%	32.6 %	36.5 %	36.2 %	34.2 %	37 %
<b>grain shape:</b>						
<b>texture</b>	regular and smooth	irregular surfaces	conchoidal fractures	conchoidal fractures	conchoidal fractures	conchoidal fractures
<b>roundness</b>	well rounded	angular	very angular	very angular	very angular	very angular
						
<b>form*</b>	1.04	1.63	2.00	2.10	2.18	2.19
<b>SH1 (H/V)</b>	1.21 / 1.19	1.52 / 1.51	1.74 / 1.75	1.79 / 1.92	1.67 / 1.65	1.83 / 1.98
<b>PARIS (H/V)</b>	3.36 / 2.83	8.55 / 8.34	6.96 / 5.43	7.57 / 9.60	3.03 / 2.78	6.79 / 7.20

X-ray attenuation values of granular materials contained in small bottles having a diameter of 42 mm are determined using a Toshiba Asteion X-ray computer tomographer. The attenuation value of a granular material (given in Hounsfield units, HU) depends mainly on its mineralogical composition, grain size and compaction (Colletta et al., 1991). The average attenuation values at 120 kV and 75 mA X-ray tube energy range from 355 HU for Pyrex to 1244 HU for brown corundum (Table 2). In order to visualise layering in X-ray CT images, adjacent materials must present differences in attenuation values of at least 100 HU.

The shape is a complex property of a grain and is analysed in detail in both descriptive and quantitative terms in order to assess its importance with regard to the mechanical behaviour of the tested materials. Descriptive terms include surface texture and roundness, whereas quantitative terms include different shape factors. The surface texture of the materials is characterised using a binocular microscope (Table 2). The surface texture of microbeads is rather regular and smooth, while

quartz sand grains display irregular surfaces. Pyrex, glass fragments and white and brown corundum mainly show conchoidal fractures, i.e. smooth surfaces and very sharp edges. Roundness is estimated by simple visual comparison of grains with standard images of known roundness using the classification of Powers (1953). The roundness of a particle depends on the sharpness of the edges and corners and is independent of the shape. Microbeads are well-rounded (snail's eggs shape), quartz sand grains have a distinct angular shape, and Pyrex, glass fragments and white and brown corundum are very angular.

Two-dimensional quantification of grain shape factors is done on thin sections of resin-impregnated granular materials analysed with a scanning electron microscope (SEM). Because of their shape, the grains have a preferred orientation in the resin. Therefore, both vertical (V) and horizontal (H) thin sections are made for each material in order to estimate the grain shape factor according to the orientation. For each thin section, four surface images are recorded at different locations.

The greyscale images obtained with the SEM are digitally enhanced, converted to binary and digitised. The form of grains is analysed using the longest and shortest diameter of a particle. The ratio of these two values defines the elongation of a grain and varies from nearly 1 for microbeads to 2.20 for glass fragments (Table 2). Two software packages, Scasmo 2.0 (Panozzo and Hürlimann, 1983) and Shape 2.0 (Panozzo, 1983) are applied to the previously digitised outlines of the grains in order to quantify the SH1 and PARIS shape factors.

Shape factor SH1 is based on comparing grain shapes to a circle. SH1 is defined as  $U^2/4\pi F$ , where  $U$  is the perimeter of the grain and  $F$  the grain's area. SH1 = 1 for a circle and increases with increasing deviation from circularity. The analysis of shape factor SH1 gives nearly similar results for both horizontal and vertical sections except for white corundum and glass fragments (values for vertical sections are 7% and 8% higher respectively). Microbeads yield the lowest value (1.19) whereas quartz sand, Pyrex, brown corundum, white corundum and glass fragments have successively higher values (Table 2), ranging between 1.51 and 1.98.

A less traditional shape factor, the PARIS factor developed by Panozzo and Hürlimann (1983), is used to obtain information on convexity or concavity of grain particles. Contrary to the SH1 shape factor, which is not able to distinguish indentations as such from strict convexity if the basic shape is not a circle, the PARIS shape factor is designed to quantify the deviations from strict convexity irrespective of the initial shape. For strictly convex shapes, i.e. circles, ellipses and squares, the PARIS factor is zero. It increases with increasing indentation. The PARIS factor is low (between 2.78 and 3.36) for both microbeads and Pyrex indicating relatively few indentations (Table 2). At first sight this result is quite surprising as microbeads and Pyrex have quite a different grain morphology. The low PARIS factor for both materials can be explained by the polygonal shape of Pyrex grains with relatively planar surfaces and the absence of irregularities in the production process of microbeads. The PARIS factor is considerably higher for glass fragments, brown corundum, white corundum and quartz sand, with values between 5.43 and 8.55.

### 3. Mechanical behaviour of the materials

Studies in soil mechanics have shown that the behaviour of granular materials is more complicated than previously assumed by most analogue modellers. The failure properties of a granular material are characterised by its coefficient of internal friction and its cohesion. The coefficient of internal friction reflects how particles slide against each other, whereas cohesion is a measure of the shear stress the material can withstand in the absence of any confining normal stress (Mandl, 1988).

Three different methods have been developed in the past to determine the mechanical properties of granular materials used in analogue modelling. The simplest one estimates the coefficient of internal friction from the orientation of fault planes relative to the maximum stress (Krantz, 1991a,b). Another method uses a shear box, the Hubbert-type apparatus (Hubbert, 1951) with which the ratio of shear stress to normal stress can be

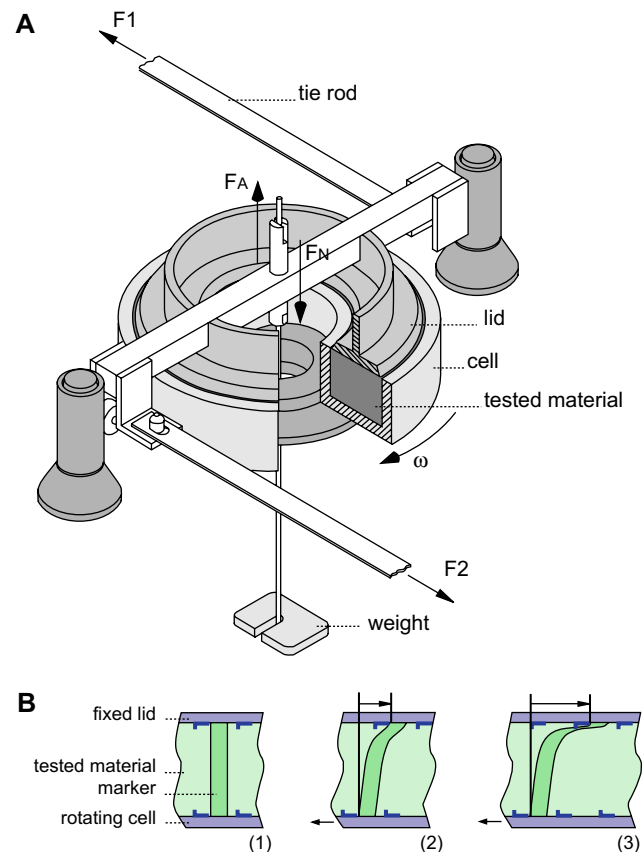


Fig. 1. Ring-shear tester. (a) Sketch of the ring-shear tester (modified from Schulze, 1994). Granular material is deposited in an annular cell. A vertical load  $F_N$  is applied through an annular lid and can be adjusted with weights. Tie rods fixed to the annular lid prevent it from rotating. During rotation of the cell (as indicated by the arrow) the shear force ( $F_1 + F_2$ ) necessary for shearing is measured. (b) Hypothetical vertical sections (aligned along the ring, not radially) of the ring-shear tester: (1) before cell rotation; (2) during cell rotation; and (3) at the end of the experiment. The hypothetical marker illustrates the shearing of the bulk sample.

determined when failure occurs (Krantz, 1991b; Schellart, 2000 and Lohrmann et al., 2003). A third method consists of measuring the stress-strain curve of granular materials using a ring-shear tester (Mandl et al., 1977; Lohrmann et al., 2003). This method allows to determine the evolution of material strength with increasing strain in more detail and with higher precision than the two previously mentioned methods. In this paper, friction coefficients and cohesion of granular materials are determined using a ring-shear tester. In addition, internal friction coefficients are calculated from the dip of fault planes in simple extensional sandbox experiments.

The ring-shear tester (RST-01, GFZ Potsdam, Germany; Schulze, 1994) allows measurements of mechanical properties under low normal loads that are in the range of stresses observed in scaled analogue experiments (Lohrmann et al., 2003). Material is sifted from a height of 30 cm into an annular cell up to a height of 4 cm with a filling rate of about 200 cm<sup>3</sup>/minute (Fig. 1a). A vertical load  $N$  is then applied by a lid fitting into the cell. The value of the load is variable and scaled according to the stresses applied in the analogue experiments. Measurements are done for different loads

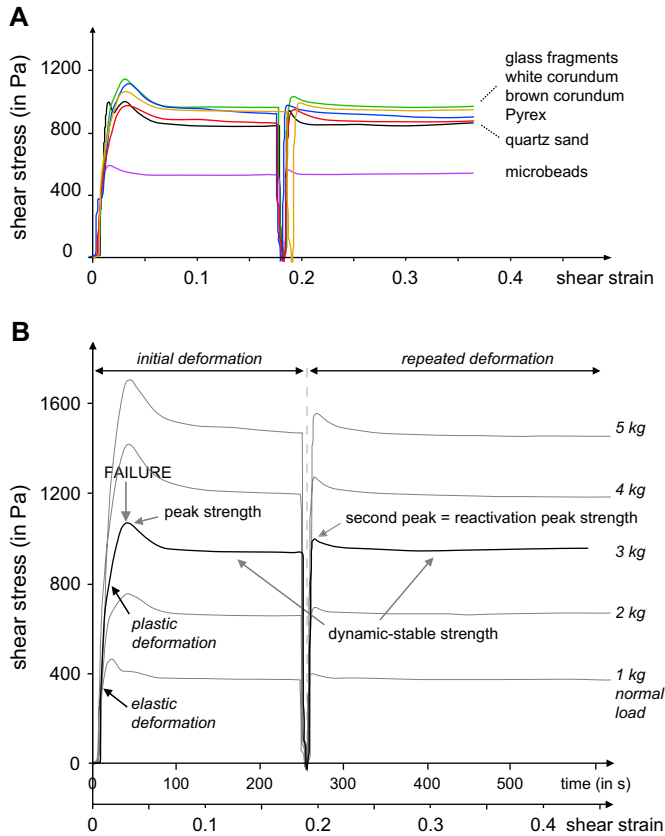


Fig. 2. Ring-shear test results. (a) Plots of shear stress as a function of angular shear strain for the tested granular materials. (b) Shear stress plotted as a function of shear strain for brown corundum. Measurements are repeated using different normal loads from 1 to 5 kg at 1 kg intervals.

ranging from 1 to 5 kg in steps of 1 kg. The cell rotates with a constant angular velocity (in direction of arrow  $\omega$  in Fig. 1a) while the lid is kept firm by two tie rods. During rotation, a horizontal shear zone develops in the granular material at the transition between the fixed lid and the rotating cell. This is illustrated in Fig. 1b through three hypothetical vertical sections perpendicular to the radius of the ring. During the test, the shear force ( $F_1 + F_2$  in Fig. 1a) acting on the tie rods is recorded through time. Each test is composed of two shear-load cycles. The first cycle tests the behaviour of non-deformed materials whereas the second one tests pre-deformed materials (Lohrmann et al., 2003). Each test is repeated at least three times to minimise measuring errors. The compressive normal stresses in our shear tests are low enough to avoid crushing of the grains.

### 3.1. Shear stress variations through time

The shear stress variation with time and with shear strain is similar for all tested granular materials (Fig. 2a) and is illustrated for white corundum at a normal load of 3 kg (solid curve in Fig. 2b). The shear stress strongly increases as white corundum is progressively deformed. The transition from initially elastic to plastic deformation is gradual (Jaeger and Cook, 1979) and can thus not be identified precisely on the graph.

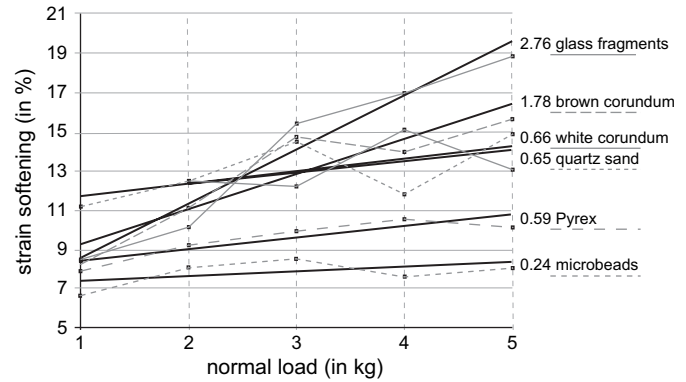


Fig. 3. Plots of strain softening (in percent) as a function of normal load for the investigated materials. The number adjacent to each granular material is a measure of the general increase of strain softening with normal load and corresponds to the slope of the straight line (solid line) obtained by linear regression analysis of the data.

A stage of plastic strain hardening precedes the onset of failure at peak strength. At this point the arrangement of the grains is perturbed along a localised shear zone. Failure at peak strength is followed by a stage of strain softening during which the shear stress decreases to reach a stable value: the dynamic-stable strength. This corresponds to the stress level necessary for faulting to remain active (stable sliding; Lohrmann et al., 2003). At this stage, the material continues to deform without further change in stresses and volume (Chu, 1995) provided the shear zone remains in its mechanically optimised orientation (Adam et al., 2005). Once this stable level has been reached, the cell rotation of the ring-shear tester is stopped and shear stress drops to zero. When cell rotation is resumed, shear stress increases once more to a second peak strength or reactivation peak strength, which is followed by a decrease to a second dynamic-stable strength. The shear stress variations of the second shear-load cycle are similar to the first cycle. The second peak strength corresponds to shear zone reactivation and occurs at a lower stress value than that required for shear zone initiation.

Ring-shear test results show that for the same normal load failure in glass fragments, white and brown corundum, Pyrex and quartz sand occurs at much higher shear stress than for failure in microbeads (Fig. 2a). With increasing normal load, the value of shear stress required to attain first peak strength, reactivation peak strength and dynamic-stable strength also increases (Fig. 2b).

### 3.2. Strain softening

Strain softening corresponds to the weakening of the shear zone and is measured as the difference between the coefficient of peak friction and dynamic-stable friction divided by the coefficient of dynamic-stable friction. Fig. 3 shows the values of strain softening in percent for each tested material plotted against normal load. At a normal load of 5 kg strain softening is lowest for microbeads (8%) and highest for glass fragments (19%). There is an overall increase of strain softening with normal load, which can be quantified by taking the slope of

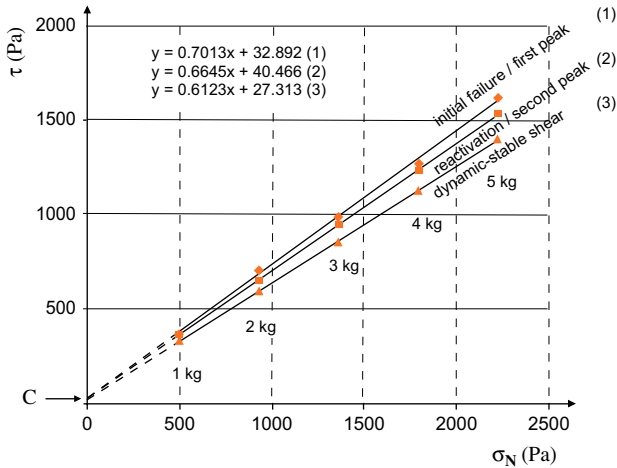


Fig. 4. Plots of shear stress ( $\tau$ ) as a function of normal stress ( $\sigma_N$ ) for quartz sand. The three straight lines obtained by linear regression analysis correspond to: (1) fault initiation at first peak strength; (2) fault reactivation at second peak strength; and (3) fault sliding at dynamic-stable strength. C is linearly extrapolated cohesion.

the straight lines obtained by linear regression analysis for each material (Fig. 3). The increase is smallest for microbeads (0.24), successively higher for Pyrex, quartz sand, white corundum and brown corundum with values of 0.59, 0.65, 0.66 and 1.78 respectively, and highest for glass fragments (2.76).

### 3.3. Internal friction coefficients and cohesion

By measuring the shear stress ( $\tau$ ) values obtained for different normal loads at first peak strength, reactivation peak strength (second peak strength) and at dynamic-stable strength, normal stresses ( $\sigma_N$ ) are calculated and plotted against the shear stresses. The plot defines Coulomb envelopes with:

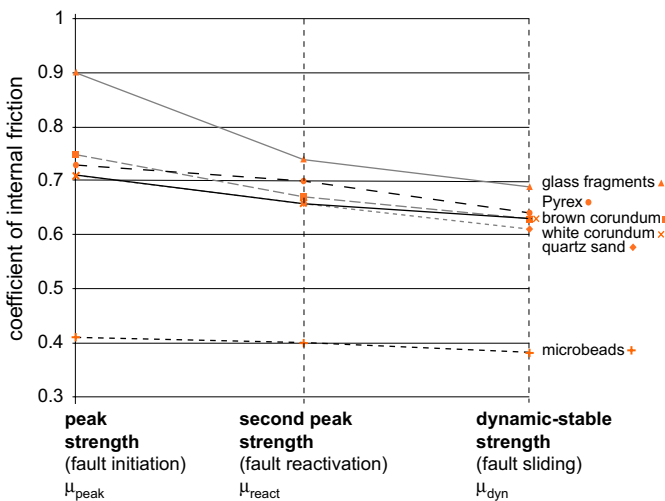


Fig. 5. Values of the coefficients of internal friction at first peak strength, second peak strength (or reactivation peak strength) and at dynamic-stable strength for different granular materials.

$$\tau = C + \mu\sigma^N$$

where C is cohesion and  $\mu$  is the coefficient of internal friction.

From these graphs, the following coefficients of internal friction can be derived from linear regression analysis of these data (Fig. 4): the coefficients of first peak friction (also referred to as peak friction,  $\mu_{\text{peak}}$ ), reactivation peak friction ( $\mu_{\text{react}}$ ) and dynamic-stable friction ( $\mu_{\text{dyn}}$ ). For each material, the coefficients of peak friction, reactivation peak friction and dynamic-stable friction are successively lower (Fig. 5). The peak friction coefficient is smallest for microbeads ( $\mu_{\text{peak}} = 0.41$ ), highest for glass fragments ( $\mu_{\text{peak}} = 0.90$ ) and has rather similar intermediate values for quartz sand, white corundum, Pyrex and brown corundum and Pyrex with peak friction coefficients of 0.71, 0.71, 0.73 and 0.75 respectively (Table 3). The cohesion (C) can be inferred from the graphs by extrapolation along a straight line to intersection with the shear stress axis. For normal stresses contained between 500 and 2250 Pa and for repeated measurements, a wide range of values is obtained for the cohesion (Table 3). At peak friction, cohesion is lowest for Pyrex ( $7 \pm 3$  Pa) and highest for white corundum ( $102 \pm 3$  Pa). Schellart (2000), however, tested different granular materials under very low normal stresses (50–900 Pa) and demonstrated that for normal stresses below  $\sim 250$ –400 Pa, the Coulomb fracture envelope deviates from a straight line and shows a convex-outward shape with cohesion converging to zero at zero normal stress. The same behaviour has also been reported from experimental data on frictional sliding (Byerlee, 1978). This suggests that the linearly extrapolated values of cohesion at normal stresses below  $\sim 400$  Pa are overestimates. At the stress range of the experiments, the materials are nearly cohesionless.

### 3.4. Basal friction

Basal friction between the horizontal base of a sandbox and overlying granular material depends both on the nature of the bottom of the sandbox and on the material. The value of the basal friction is a key parameter in analogue modelling and it can be varied by using different kinds of sandbox bottom-plates such as wood, plastic, PVC or sandpaper. The basal friction is measured using the ring-shear tester. A basal plate consisting of either wood, PVC or plastic is fixed at the bottom of the ring-shear tester cell and covered by a 1-cm-thick layer of granular material. The coefficients of basal friction for quartz sand, brown corundum and microbeads overlying different types of bottom-plates are given in Table 4. The data show that basal friction coefficients are higher when the basal plate is made of wood instead of plastic or PVC.

A 1-mm thin layer of microbeads between bottom plate and overlying granular material reduces basal friction considerably. In case of quartz sand or brown corundum overlying the microbeads, basal friction decreases by 37% and 57%, respectively. The thin layer of microbeads also reduces the reactivation peak strength to almost the level of the dynamic-stable strength, i.e. resumption of basal sliding is facilitated.

Table 3  
Angles and coefficients of internal friction, and linearly extrapolated cohesion (in Pa) obtained with a ring-shear tester for different granular materials. The extrapolated cohesion of glass fragments is negative

Sifted material	Angle ( $\phi$ ) and coefficient ( $\mu$ ) of internal friction			Apparent cohesion (Pa)			
		First peak	Second peak	Dynamic-stable	C1 (first peak)	C2 (second peak)	C3 (dynamic-stable)
Quartz sand	$\phi$	35.5°	33.3°	31.2°	21 ± 18	34 ± 4	49 ± 10
	$\mu$	0.714 ± 0.020	0.657 ± 0.006	0.607 ± 0.005			
Brown corundum	$\phi$	37°	33.8°	32.2°	39 ± 10	66 ± 9	65 ± 9
	$\mu$	0.754 ± 0.017	0.669 ± 0.008	0.629 ± 0.006			
White corundum	$\phi$	35.6°	33.6°	32°	102 ± 3	74 ± 5	72 ± 7
	$\mu$	0.716 ± 0.008	0.665 ± 0.002	0.626 ± 0.001			
Glass fragments	$\phi$	42°	36.5°	34.7°	—	38 ± 3	34
	$\mu$	0.900 ± 0.005	0.739 ± 0.004	0.692 ± 0.001			
Pyrex	$\phi$	36.2°	35.1°	32.7°	7 ± 3	25 ± 3	17 ± 3
	$\mu$	0.731 ± 0.002	0.703 ± 0.003	0.643 ± 0.001			
Microbeads	$\phi$	22.3°	21.9°	20.6°	25 ± 4	25 ± 3	27 ± 3
	$\mu$	0.410 ± 0.188	0.402 ± 0.133	0.376 ± 0.080			

### 3.5. Internal friction coefficients determined from fault dips

Extensional analogue experiments are done to determine internal friction coefficients ( $\mu$ ) of different granular materials from fault dip measurements. The internal friction coefficient is related to the angle ( $\theta$ ) between the pole of a fault and the maximum principal stress direction (Krantz, 1991a,b) by the relation:  $\mu = \tan(2\theta - 90^\circ)$ . The experiments are done in a rectangular sandbox in which granular materials are sifted from a height of 30 cm. A plastic sheet underlies part of the model and is fixed to the mobile wall. Prior to extension the model is 25 cm long, 11.5 cm wide and 3 cm thick. Outward displacement of the mobile wall results in the formation of a symmetric graben above the lateral end of the plastic sheet which represents a velocity discontinuity. Fault inception and evolution is analysed using successive X-ray CT cross-sectional images taken at 1 mm increments of displacement. To avoid edge effects, fault dip measurements are made in cross-sections away from the side walls of the sandbox. As will be discussed in more detail later on, X-ray CT images show that the initial

fault shape is not rectilinear in cross-section but curved. The internal friction coefficient is therefore determined from the fault dips measured directly above the velocity discontinuity where the conjugate faults initiate and where the vertical normal stress equals the overburden weight and corresponds to the maximum principal stress ( $\sigma_1$ ). Thus, the internal friction coefficient corresponds to the one at peak strength ( $\mu_{\text{peak}}$ ). Table 5 gives the results of the fault dip tests.

For sifted materials, the coefficient of peak friction is highest for glass fragments ( $\mu_{\text{peak}} = 1.73$ ; corresponding normal fault dip is 75°) and successively lower for white corundum ( $\mu_{\text{peak}} = 1.6$ ; 74°), quartz sand ( $\mu_{\text{peak}} = 1.28$ ; 71°), Pyrex and brown corundum ( $\mu_{\text{peak}} = 1.19$ ; 70°), and microbeads ( $\mu_{\text{peak}} = 0.67$ ; 62°). The coefficient of peak friction of poured quartz sand is 0.62 (corresponding normal fault dip is 61°) and is lower than for all sifted materials.

## 4. Discussion

The science of granular media has a long history with much engineering literature devoted to understanding the

Table 4  
Angles and coefficients of basal friction obtained with a ring-shear tester for different granular materials

Sifted material	Angle and coefficient of basal friction			
		First peak	Second peak	Dynamic-stable
Quartz sand/wood	$\phi$	28.3°	29.5°	28.3°
	$\mu$	0.538 ± 0.008	0.566 ± 0.004	0.538 ± 0.008
Quartz sand/PVC	$\phi$	20.7°	20.8°	20.7°
	$\mu$	0.378 ± 0.010	0.381 ± 0.009	0.378 ± 0.010
Quartz sand/plastic	$\phi$	20.7°	24.9°	21.3°
	$\mu$	0.377 ± 0.003	0.464 ± 0.033	0.39 ± 0.028
Quartz sand/microbeads/plastic	$\phi$	13.1°	12.2°	12.2°
	$\mu$	0.233 ± 0.003	0.216 ± 0.006	0.216 ± 0.006
Brown corundum/plastic	$\phi$	29.5°	28.5°	28.5°
	$\mu$	0.566 ± 0.003	0.542 ± 0.003	0.542 ± 0.008
Brown corundum/microbeads/plastic	$\phi$	12.6°	12.6°	12.5°
	$\mu$	0.224 ± 0.010	0.223 ± 0.004	0.223 ± 0.010
Microbeads/plastic	$\phi$	13.8°	12.9°	12.6°
	$\mu$	0.245 ± 0.088	0.228 ± 0.010	0.224 ± 0.080

Table 5  
Coefficients of internal peak friction obtained (1) from fault dip measurements in extensional experiments and (2) using a ring-shear tester

	Extensional experiments			Ring-shear tester	
	Normal fault dip	$\mu_{\text{peak}}$	$\phi_{\text{peak}}$	$\mu_{\text{peak}}$	$\phi_{\text{peak}}$
Poured quartz sand	61°	0.62	32°	—	—
Sifted material					
Quartz sand	71°	1.28	52°	0.71	35.5°
Brown corundum	70°	1.19	50°	0.75	37°
White corundum	74°	1.60	58°	0.76	35.6°
Glass fragments	75°	1.73	60°	0.90	42°
Pyrex	70°	1.19	50°	0.73	36.2°
Microbeads	62°	0.67	34°	0.41	22.3°

mechanical behaviour of these materials (e.g., Jaeger et al., 1996). Granular materials have a rich set of unusual behaviour which prevents them from being simply categorised as either solids, fluids (Mueth et al., 1998) or gas. These materials sometimes behave like either of the 3 states or even different from any (Lätzel, 2003). In granular materials, applied forces propagate along the contacts between the grains through ‘force chains’ (Hartmann et al., 2002). At each grain, the force lines bifurcate into several branches and can turn by 180° and, therefore, the propagation of forces through the packing goes along a (kinky) tree-like structure (Herrmann, 2001). Because of the nature of force transmission, there are strong fluctuations of the forces inside a granular assembly which is thus quite inhomogeneous (Lätzel, 2003).

The shear stress variations recorded by the ring-shear apparatus allow the identification of the successive stages of deformation of a granular sample. The evolution of the internal

structure of granular materials, the thickness and dip of shear zones during deformation in simple sandbox experiments are described in the light of the combined analysis of the physical and mechanical properties of the granular materials and with the help of a X-ray CT scanner.

4.1. Diffuse deformation

Lohrmann et al. (2003) show that the process of early, diffuse deformation associated with sample compaction in shear tests is followed by a stage of dilatancy prior to failure. The compaction/decompaction cycle is linked to shear stress variations recorded during the deformation of a granular material performed in a ring-shear tester (Lohrmann et al., 2003; Fig. 6). The maximum decompaction rate corresponds to peak strength whereas the transition to dynamic-stable strength is associated with a decrease in the decompaction rate (Mandl, 1988; Lohrmann et al., 2003).

When submitted to shear, the grains are rearranged in such a way that they become tightly packed during the compaction phase. In this dense granular pack, grains accommodate stresses by sliding past each other and/or through rotations. When two grains get stuck, they exert great forces on the surrounding medium generating a collective displacement of grains in order to unlock the two grains (Herrmann, 2001)

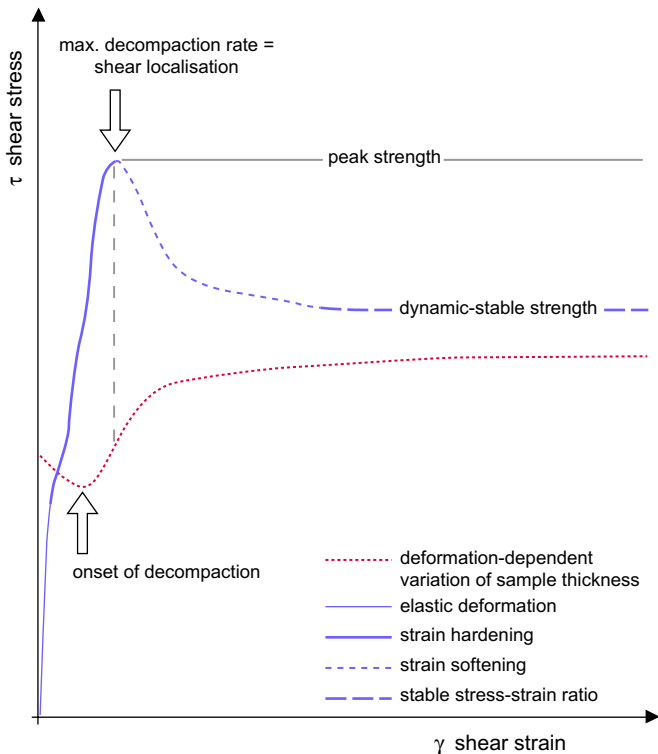


Fig. 6. Plot of shear stress as a function of shear strain for granular material (modified from Lohrmann et al., 2003).

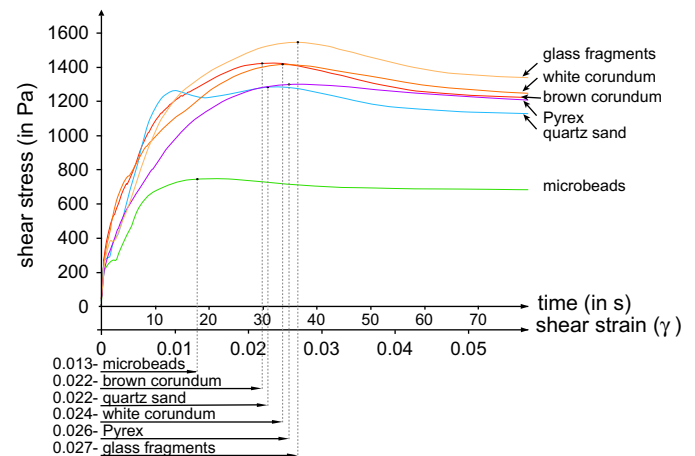


Fig. 7. Shear stress plotted as a function of time and shear strain during ring-shear testing with a normal load of 4 kg. Depending on the material, failure at peak strength occurs at a different amount of shear strain.



and thus leading to decompaction of the material. As demonstrated by Lätzel (2003), compressed granular materials need to dilate before being able to deform.

In sheared granular materials, the load is supported in part by sets of particle chains or stress chains which are transient and collapse by interparticle slip or rolling during shearing (Mair et al., 2002). The nature of stress chains depends on grain characteristics and interactions such as the number of other grains contacting each particle (number  $Z$ ). This number  $Z$  increases with particle roughness and particle size distribution range (Mair et al., 2002). Small  $Z$  values correspond to localised stress chains, whereas large  $Z$  values imply diffuse stress chains. Mair et al. (2002) propose that in granular materials having localised stress chains, particles have a high probability of failure owing to high individual contact stresses. In case of diffuse stress chains, however, the load is distributed over many particles, reducing stresses at individual contacts and making failure less likely.

The ring-shear tests show that the amount of shear strain required to reach peak strength and thus to initiate faults depends on the type of granular material (Fig. 7) and on the handling technique. The interval between the onset of shear strain in the ring-shear tests and incipient failure corresponds to diffuse deformation and is smallest for microbeads and largest for glass fragments. The high sphericity and roundness of microbeads combined with their low porosity and low SHI and PARIS shape factors suggests that these particles accommodate stresses prior to failure mainly by particle rotation and less by sliding. The fact that the density values of microbeads show little dependence on the handling technique used – density of sifted microbeads is only slightly higher than of poured microbeads – indicates that the particles have a nearly cubic close packing arrangement and thus a limited grain-rearrangement potential. The internal reorganisation preceding failure is small and deformation remains highly confined. Microbeads seem to accommodate shearing through localised particle chains, which are quite unstable and thus fail easily. In contrast, glass fragments undergo more diffuse deformation than microbeads (Fig. 7). The grain-rearrangement potential of glass fragments is higher than for microbeads because of their elongated and irregular shape. Density of sifted glass

fragments is much higher than for poured glass fragments (1.24 and 1 g/cm<sup>3</sup>, respectively). Once compacted, the grain characteristics of glass fragment particles (angular shape with conchoidal fractures, elongated and indented) do not allow the grains to simply accommodate stresses by rotation. Stresses are dissipated through the glass fragment pack resulting in decompaction. Similar conclusions are reached by Kruyt and Rothenburg (2004) who demonstrate an increase in dilatancy with friction coefficient and thus with irregularity of grain shape.

Grain size distribution seems to be an additional factor, which could influence the amount of diffuse deformation that a material can undergo before failure. As demonstrated by Antonellini et al. (1994) many particles of different size distribute stresses at many points of contact, while similar particles concentrate stresses at fewer points of contact (Mair et al., 2002). This could explain the large amount of diffuse deformation for white corundum, Pyrex and glass fragments with their more heterogeneous grain size distributions as compared to microbeads, quartz sand and brown corundum. Failure in white corundum, Pyrex and glass fragment is reached at a higher amount of shear strain as the wider grain size range results in higher dispersion of stresses through the material pack.

#### 4.2. Localisation of deformation and shear zone inception

With increasing shear strain, granular materials start to develop shear bands rather than deforming uniformly. The process which gives rise to shear bands is known as “strain localisation” and occurs at, or shortly before peak strength (Desrues and Viggiani, 2004). These shear bands are dilatant zones in which the grain arrangement is perturbed and deformation localizes. The dilatancy inside the shear bands has been measured by Herrmann (2001), Colletta et al. (1991) and Desrues (2004) using a CT scanner. It has been observed in plane strain experiments that near peak strength, several incipient shear bands can appear simultaneously but that only one will develop fully (Desrues, 2004).

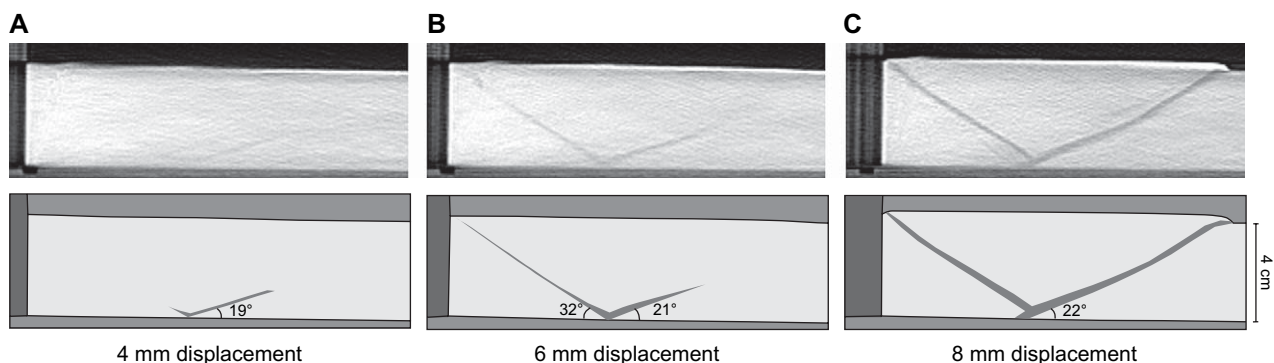


Fig. 8. X-ray CT images and corresponding line drawings of early fault evolution in experiment after 4 mm (a); 6 mm (b); and 8 mm (c) of shortening. Undeformed model consists of a 4-cm-thick layer of quartz sand.

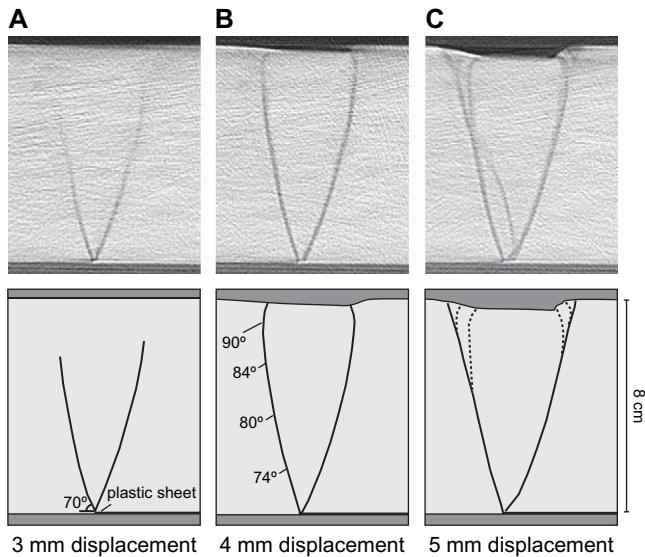


Fig. 9. X-ray CT images and corresponding line drawings of early fault evolution in analogue experiment after 3 mm (a); 4 mm (b); and 5 mm (c) of extension. Undeformed model consists of a 8-cm-thick layer of quartz sand.

The extension experiments described in Section 3.5 and additional shortening experiments are used to investigate shear zone inception in quartz sand. In the shortening experiments, a rectangular box with a horizontally movable wall is filled with 3 cm of sand. Inward displacement of the mobile wall results initially in lateral compaction and diffuse deformation of the model. No localized deformation is visible in X-ray CT images until 4 mm of displacement, when the deformation localises in narrow conjugate zones (Fig. 8a). These zones are visible because of the associated dilatancy that results in lower density and thus in a reduction of the X-ray attenuation compared to the surrounding material. At 4 mm of displacement, the conjugate dilatant zones do not yet show any visible offset and are considered as precursor shear zones that form at or just prior to failure at peak strength. With increasing displacement

of the mobile wall, these precursor shear zones become broader, propagate upward (Fig. 8b) and turn into conjugate reverse shear zones (thrust faults; Fig. 8c). The dip of the backthrust is steeper than the dip of the forward thrust. The forward thrust itself steepens upward, dipping  $23^\circ$  at the base and  $31^\circ$  near the surface. The asymmetry in dip angle of the conjugate thrusts and the listric shape of the forward thrust is caused by friction at the base of the sandbox that results in a slight deflection of the  $\sigma_1$  trajectories from horizontal as demonstrated by Hubbert (1951) and Mandl (1988). As the listric forward thrust reaches the surface it flattens out and thus becomes sigmoidal in profile.

In the extensional experiments, the thickness of the sandpack is varied (2, 3, 4 and 8 cm). In each experiment conjugate dilatant zones (precursor faults) initiate at the lateral edge of the plastic sheet after 1–2 mm of displacement of the mobile wall (Fig. 9a). With increasing extension, the conjugate precursor fault system acquires a “tulip” shape, i.e. both precursor faults steepen as they propagate upward (Fig. 9b). At 4 mm of extension offset along the dilatant zones is visible in X-ray CT images and the dip angle of the conjugate faults increases from about  $70^\circ$ – $73^\circ$  at the base to  $90^\circ$  at about 5–9 mm below the surface independent of the initial model thickness (Fig. 10). In the upper few mm of the sandpack, the dip direction of the conjugate fault switches. As a consequence, the uppermost segments of the conjugate faults have the character of upward convex reverse faults.

The resolution of the CT images does not permit to determine if there is dependence of fault dip angle at the base on model thickness. Faults dip at about  $70^\circ$ – $73^\circ$  at the base of the model. However, we observe that in all extensional experiments the early faults become vertical just below the surface at a depth of about 6–9 mm independent of model thickness. This observation allows us to make inferences on the shape of the failure envelope. At normal stresses of at least 300 Pa (corresponding to an overburden of 2 cm), the failure envelope is approximately linear and therefore faults at the base will initiate at similar angles. However, at very low normal stresses

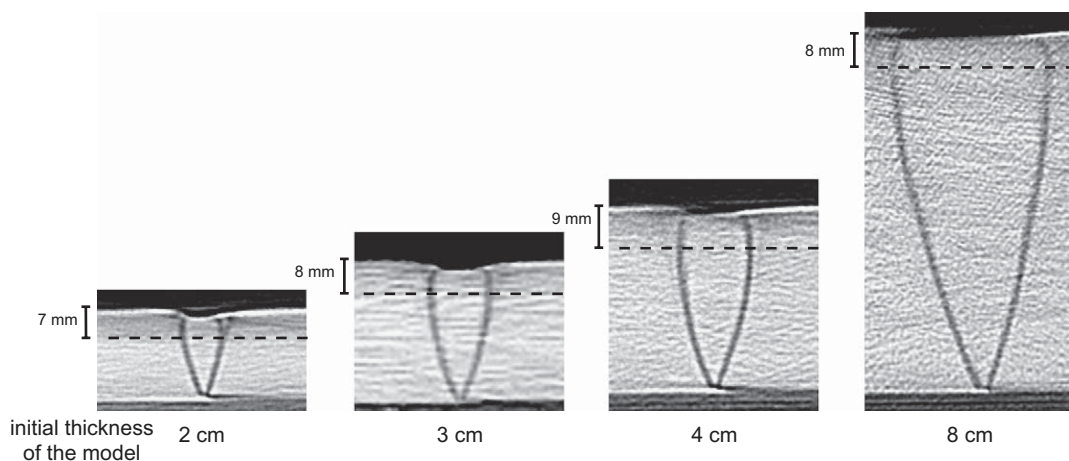


Fig. 10. Comparison of early fault evolution in quartz sand models undergoing extension. Initial model thickness is either 2, 3, 4 or 8 cm. Note the upward steepening of the faults and overturned segments just below the surface. Early faults are vertical at about 7–9 mm below the surface independent of initial model thickness.

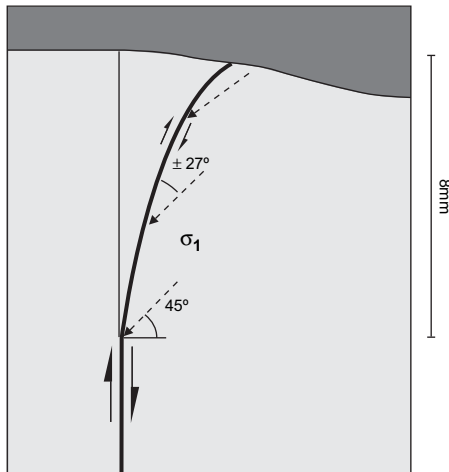


Fig. 11. Schematic line drawing of uppermost segment of early fault in extension experiment. Fault is shown by thick solid line. Inferred orientations of the maximum principal compressive stress are indicated by dashed arrows. Half-arrows indicate relative displacement along fault.

below  $\sim 300$  Pa the failure envelope is no longer linear but convex-outward. The failure envelope intersects the normal stress axis at nearly a right angle for normal stresses close to zero. Mandl (1988) shows that effective normal stresses cannot become tensile in loose, unconsolidated and nearly cohesionless granular materials and therefore faulting cannot be tensile. Thus, for very low normal stresses below  $\sim 300$  Pa, the coefficient of internal friction tends towards infinity and the dip of the normal faults increases to  $90^\circ$  at shallow depths. Using a Hubbert-type shear box, Schellart (2000) also showed that at normal stresses below  $\sim 250$ – $400$  Pa the failure envelope for granular materials such as quartz sand is convex-outward.

Extension in our sandbox experiments is accompanied by tectonically induced changes in the stress field and consequently by local changes of the principal stress orientations. Offset along the vertical portion of the fault just below the surface results in shear stresses that deflect  $\sigma_1$  from vertical (Mandl, 1988). The deflected  $\sigma_1$  trajectory (Fig. 11) transects the vertical portion of the fault at  $45^\circ$  and the newly formed fault segment becomes upwards-convex as it propagates to the surface and consequently shows reverse offset. During further extension, the lower segment of each conjugate fault continues to be active, but in its upper part, new faults cut into the footwall of the pre-existing, upward steepening and overturned faults. The near vertical and reverse fault segments near the surface are in an unfavourable position for continuous sliding and a footwall short-cut develops. As extension continues, the footwall short-cut fault itself steepens upward and also becomes upward convex near the surface (e.g., Fig. 9c). At 5 mm displacement of the mobile wall, the active parts of the conjugate fault system are major normal faults with abandoned vertical and reverse fault segments in their hanging-walls.

Similar observations have been made in nature along the Paeroa Fault (Villamor, pers. comm.) and along the Kerepehi fault (Persaud, pers. comm.) in the Taupo Volcanic Zone of the Northern Island of New Zealand. The area undergoes

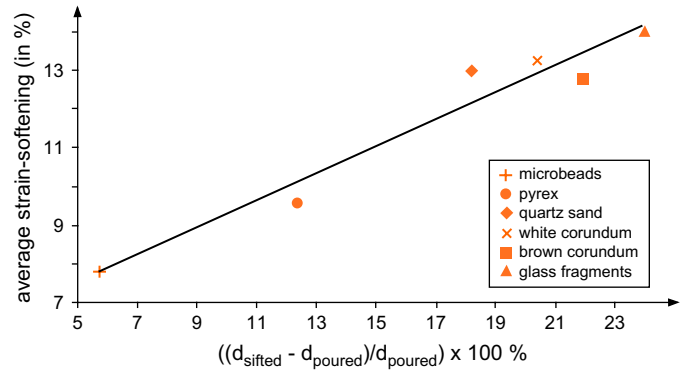


Fig. 12. Plot of average strain softening (in %) as a function of the relative difference in density between sifted and poured sand (in %) for different granular materials.

extension and trenches across major normal faults show vertical and reverse fault segments in the upper few meters in poorly consolidated sediments. A similar fault shape evolution as in our experiments has been observed in extensional wet sandbox experiments using rigid basement blocks and analysed with a high-resolution optical correlation technique (PIV, Particle Image Velocimetry) that provides detailed temporal patterns of strain accumulation (Adam et al., 2005).

#### 4.3. Strain softening

Strain localisation in granular materials at or just prior to peak strength is followed by strain softening associated with the complete development of a single shear band. The strain softening varies between the tested granular materials and generally increases with normal load (Fig. 3). This suggests that strain softening along a fault is a function of the overburden. Thus, lower portions of faults are expected to have larger strain softening than the upper portions and are hence likely to be more easily reactivated.

Fig. 12 shows a plot of strain softening against the relative difference in density between sifted and poured material. The approximately linear relation in this diagram suggests that the amount of strain softening is related to the grain-rearrangement potential of a material, i.e. to the compaction and decompaction cycle. The more a material compacts during the early phases of diffuse deformation, the more it subsequently needs to decompact (dilate) prior to failure resulting in higher strain

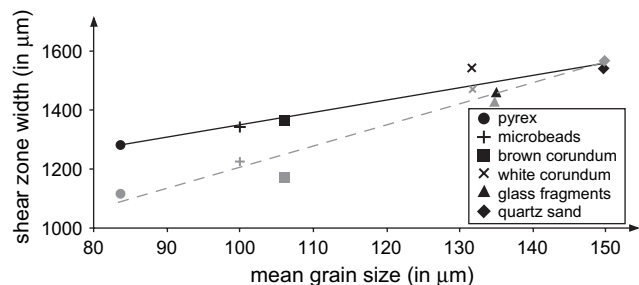


Fig. 13. Plot of initial shear zone width in extensional (black symbols) and shortening (grey symbols) experiments as a function of mean grain size for the tested granular materials.

softening along the shear zone. Although microbeads and Pyrex have a very different sphericity and SH1 shape factor, they both have a much lower strain softening than the other materials. Both microbeads and Pyrex have a low grain-rearrangement potential as indicated by the small difference in density between sifted and poured material. The arrangement of microbeads is near to a cubic close packing arrangement, whereas the granular assembly (network) of Pyrex grains is particularly rigid having a stable particle arrangement. Thus, these two materials compact little during initial strain hardening and therefore show limited strain softening after failure.

An additional parameter that could contribute to the limited strain softening of both microbeads and Pyrex is the low PARIS factor of these two materials. The other investigated materials with higher strain softening values all have considerably higher PARIS factors. A low PARIS factor implies only subdued particle indentations and therefore sliding along the fault zone in Pyrex and microbeads is easy. Consequently, the shear stress required to continue sliding along the fault plane is nearly the same as the shear stress needed to create a fault at peak strength. Once failure has occurred, displacement on the shear plane will depend on the roughness of the material particles (Nicolas, 1987) and thus mainly on the PARIS factor.

#### 4.4. Shear zone width

The width of shear zones is determined in extension and shortening experiments at the moment when offset along dilatant zones is visible in X-ray CT images, i.e. at or just after failure at peak strength. Fig. 13 shows the initial shear zone width for the six tested granular materials plotted as a function of their mean grain size. Although the initial shear zone widths of different granular materials with different grain shapes and grain size distributions are plotted in Fig. 13, the diagram suggests a dependency of initial shear zone width on mean grain size. The larger the mean grain size, the larger the initial width of the shear zone. The normalized shear zone width (i.e. the ratio of shear zone width and mean grain size) is rather uniform and varies between 11 and 16 times the mean grain size. It is emphasized that the shape, width and orientation of the initial shear zone does not remain constant but evolves during further deformation after peak failure.

In the literature a number of publications report on shear zone width in granular materials as a function of mean grain size using a plane strain biaxial compression apparatus. In these laboratory tests, the width of the shear zone is about 7–8 times (Oda and Kazama, 1998), 10 times (Roscoe, 1970), 13 times (Vardoulakis and Graf, 1985) or 18.5 times (Vardoulakis et al., 1985) the mean particle size. Although our results agree broadly with the published data, a direct comparison of our results with these published data is problematic because of uncertainties at which stage of the plane strain test the width of the shear zone was measured. Viggiani et al. (2001), however, are able to capture the onset of shear zone localisation in plane strain compression tests using false relief stereophotogrammetry. Their results confirm that shear

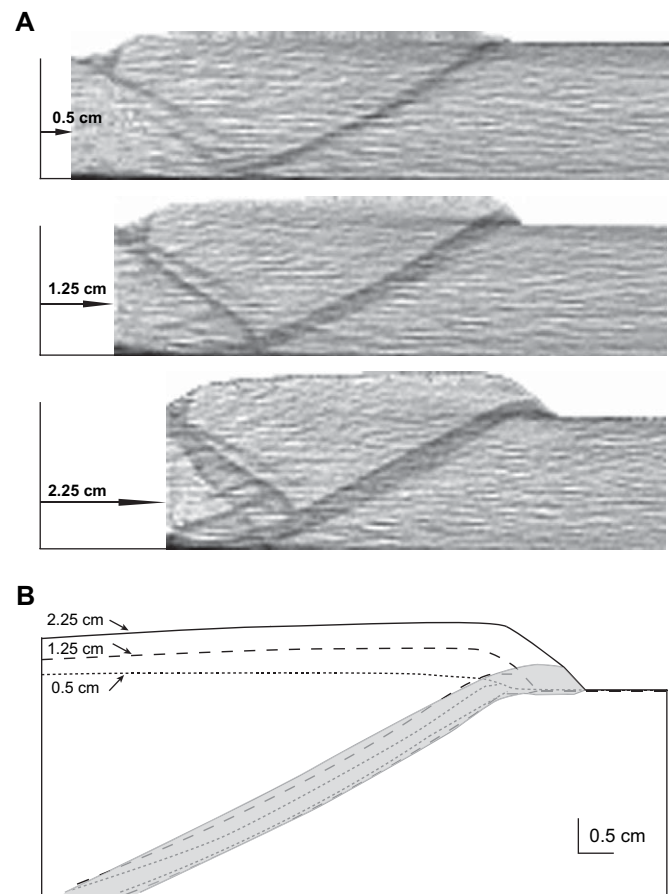


Fig. 14. Shear zone broadening in shortening experiment using quartz sand. (a) Shear zone evolution at 0.5 cm, 1.25 cm and 2.25 cm shortening. Initial model thickness is 3 cm. (b) Comparison of shear zone width at three successive stages. Note that broadening occurs progressively into the hanging-wall. Only the central part of the model is shown.

zone width at initiation depends on the mean grain size as suggested by our experiments. Mokni (1992) reports that normalized shear zone width in sand is not constant, but tends to decrease from about 20 for a grain size of 350  $\mu\text{m}$  to a constant limit value of about 7 for grain sizes of 2400 and 3200  $\mu\text{m}$ .

Our results agree rather well with theoretical analyses of shear band formation, which suggest that the width of a shear zone at initiation is about 10 times (Herrmann, 2001) or 16 times (Mühlhaus and Vardoulakis, 1987) the mean grain size. Herrmann (2001) suggests that the nature of force transmission in a granular packing results in the collective displacement of grains in a few layers giving rise to a particular width at shear zone initiation. Herrmann (2001) demonstrates that according to this mechanism and using statistics, about 5 layers may be mobilised on both sides of the initial shear plane, which is thus estimated to have a width of about 10 times the grain size diameter.

X-ray CT analysis of shortening experiments shows that the shape, orientation and width of the thrusts that form at peak failure evolve during further deformation. The forward shear steepens upward as it propagates from the basal flat to the surface and thus acquires a slightly listric shape in section (Fig. 8). As indicated before, the slightly listric shape of the

forward shear is a result of friction at the base of the sandbox. As deformation progresses, the forward shear straightens and at the same time broadens (Fig. 14a). This may be the result of progressive advection of material (including backthrusts) along the transition from lower flat to ramp, which may trigger additional deformation parallel to the existing forward shear.

In a thrust experiment with quartz sand, the initial forward shear zone width is about 11 times the mean grain size. However, as displacement along the forward shear continues, the shear zone broadens progressively into the hanging-wall (Fig. 14b). Upon cessation of displacement along the forward shear, the final width has increased to about 35 times the mean grain size. Shear zone broadening of forward shears was previously observed by Ellis et al. (2004) in the same kind of experiment.

#### 4.5. Peak friction coefficients

The coefficient of peak friction reflects how grain particles will slide against each other as a shear zone forms and is thus related to the physical characteristics of the granular material. For example, the ring-shear tests show that the coefficient of peak friction for microbeads is lower than for glass fragments, i.e. less shear stress is needed to form a shear zone in microbeads than in glass fragments, because the microbeads are smooth, well rounded, nearly spherical and have low SH1 and PARIS shape factors. In contrast, glass fragments are elongated and very angular and have high SH1 and PARIS shape factors and more shear stress is needed to create a shear zone.

The coefficient of peak friction and thus fault dip of one particular granular material also depends on the physical handling technique employed in the sandbox experiments (sifting or pouring). This dependency is observed in both the extensional analogue experiments and in the ring-shear tests. For example, sifted quartz sand has a higher coefficient of peak friction than poured quartz sand, and normal fault dips in extensional analogue experiments are about  $10^\circ$  higher in sifted sand than in poured sand. The dependency of the coefficient of peak friction on the physical handling technique has been demonstrated in previous studies (Hubbert, 1951; Krantz, 1991a,b; Schellart, 2000; Lohrmann et al., 2003). Sifted material has a lower porosity (and thus higher density) than poured material and the ability of grains to rearrange by sliding or rotation in response to the applied normal load is less than for poured material. As a consequence, the amount of shear stress needed to attain failure in sifted material increases more rapidly with increasing normal load resulting in a higher internal friction coefficient.

For sifted granular materials the coefficient of peak friction calculated from fault dip measurements in extensional analogue experiments is systematically higher than the coefficient of peak friction determined for the same material with a ring-shear tester (Table 5). The large discrepancy suggests that it can not just be explained by potential small differences in the physical handling technique employed to deposit the granular material. Instead, the differences in coefficients of peak friction can be explained by the distinct experimental set ups

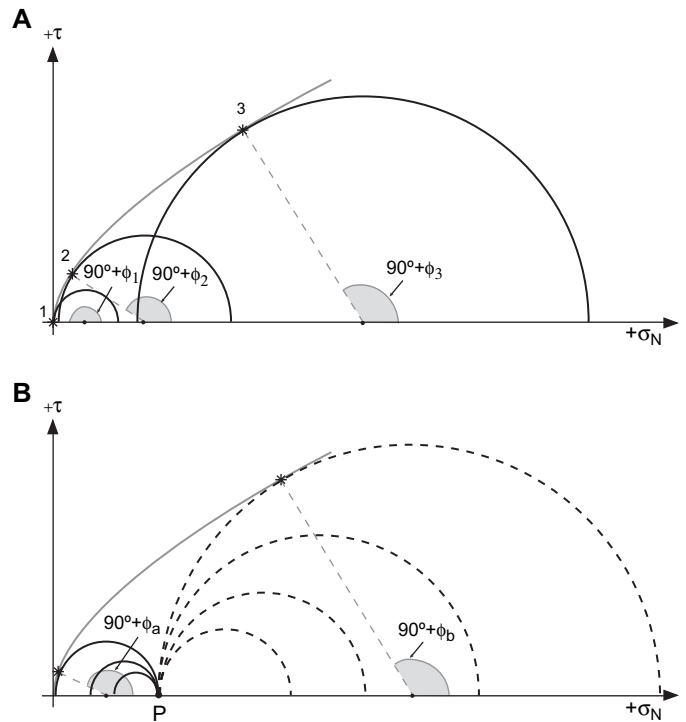


Fig. 15. (a) Mohr diagram and convex-outward failure envelope at very low normal stresses (below about 500 Pa) as inferred from the early fault evolution in extensional analogue experiments. Fault dip angles in these experiments steepen progressively upward suggesting that the angle of internal friction ( $\phi$ ) increases with decreasing overburden. Angles  $\phi_1$ ,  $\phi_2$  and  $\phi_3$  correspond to the angles of internal friction at failure. (b) Qualitative Mohr diagram at very low normal stresses showing variations in horizontal stress relative to vertical stress for contractional (larger series of stippled circles) and extensional analogue experiments (smaller series of solid circles) with identical model material and model dimensions. Point P represents the initial stress state at the base of the model. Angles  $\phi_a$  and  $\phi_b$  correspond to the angles of internal friction at failure in extension and shortening experiment, respectively. Note that for a convex-outward failure envelope  $\phi_a > \phi_b$ .

and by taking into account that for small normal stresses the failure envelope for granular materials appears not to be linear, but convex outward, resulting in a successively higher coefficient of peak friction with decreasing normal stress (Fig. 15a). Provided that model material and model dimensions are identical, failure in an extensional experiment will then occur at a lower critical shear stress and normal stress than failure in a shortening experiment (Fig. 15b) or ring-shear tester and consequently, the angle of peak friction ( $\phi$ ) and thus the coefficient of peak friction will be higher in extension experiments.

## 5. Conclusions

Our analysis of different natural and artificial granular materials using analogue experiments, grain characterisation and ring-shear tests provides insights on the mechanical behaviour of granular materials and permits to draw the following main conclusions.

- (1) Ring-shear tests show that the investigated granular materials are characterised by an initial stage of elastic strain, followed by plastic strain-hardening prior to the onset of

- failure at peak strength. Failure of the granular materials results in a perturbed arrangement of grains along a localised shear zone with associated dilatation. Failure is followed by a stage of strain-softening until a stable value referred to as dynamic-stable strength is reached.
- (2) The development of a shear zone is preceded by a phase of diffuse deformation. The amount of diffuse deformation depends on grain shape, physical handling technique and grain size distribution. Very angular elongated particles with high SH1 and PARIS shape factors undergo more diffuse deformation than highly spherical particles with low SH1 and PARIS shape factors. Diffuse deformation becomes more important when a particular material is sifted instead of poured. The amount of diffuse deformation also tends to be larger with increasing grain size heterogeneity.
  - (3) Strain softening generally increases with increasing normal load suggesting that fault weakening increases with depth. The increase in strain softening with normal load is lowest for materials which show limited compaction and have a low grain-rearrangement potential (as evidenced by the small difference in relative density between their sifted and poured state). A low PARIS shape factor and thus little particle indentations may also contribute to limited strain softening.
  - (4) X-ray CT analysis of analogue experiments shows that diffuse deformation is followed by localized deformation along narrow, dilatant zones. These zones are interpreted as precursor shear zones forming at or just prior to failure at peak strength. Early faults in extensional experiments initiate at the base, steepen upward and become vertical several mm below the surface. This fault evolution suggests a gradual increase in the coefficient of internal peak friction with decreasing normal stress (overburden) at very small normal stresses (below about 300 Pa), and would indicate that the failure envelope for this small normal stress range is convex outward. Further extension in these experiments results in local modifications of the principal stress orientations in the upper few mm of the model, with short-lived steep and even reverse fault segments.
  - (5) Initial shear zone width in analogue experiments increases with mean grain size and varies between about 11 and 16 times the mean grain size. These values are broadly comparable to those determined in plane strain compression tests and to those calculated from theoretical analyses on shear band formation. During further deformation shear zones broaden progressively until displacement ceases.
  - (6) The coefficient of peak friction is related to physical characteristics of the granular materials such as texture, roundness and grain shape. The coefficient of peak friction also shows a dependency on the physical handling technique (sifting or pouring).
  - (7) Coefficients of peak friction determined from fault dips in extensional experiments are systematically higher than those determined on the same material with a ring-shear tester. This difference can be explained by the distinct experimental setups and an outward convex failure envelope for granular materials at low normal stresses.
  - (8) The use of analogue materials with different coefficients of internal friction and thus different relative strengths may be used to study fault refraction in a sedimentary sequence consisting of alternating rock strengths.
  - (9) Quartz sand, brown corundum, white corundum and Pyrex can be used to model deformation in competent rocks since their coefficients of internal friction are comparable to those determined experimentally for upper crustal rocks such as sandstones and limestones. Weak microbeds can be used to model less competent rocks such as (undercompacted) shales.
  - (10) Quartz sand, brown corundum, white corundum and Pyrex can be used to visualise layering in models analysed with an X-ray CT scanner as they have almost the same mechanical properties but attenuation values that differ by at least 100 Hounsfield Units.

### Acknowledgements

Funding by the Swiss National Science Foundation (project number 2000-067952.02) is gratefully acknowledged. J. Lohrmann and J. Adam are thanked for the use of the ring-shear tester at GFZ Potsdam, M. Herwegh for use of the SEM and help with image analysis software, H. Haas for help in pycnometer and granulometric analysis, V. Greco for the thin sections, A. Liechti and H.P. Bärtschi for technical assistance, J.M. Mengus (IFP) for providing the Pyrex sample, Prof. P. Vock for use of the X-ray scanner at the Inselspital in Bern, and C. Somasundaram for help in CT data acquisition. We thank Jo Lohrmann and Juergen Adam for their constructive reviews.

### References

- Adam, J., Urai, J., Wienecke, B., Oncken, O., Pfeiffer, K., Kukowski, N., Lohrmann, J., Hoth, S., Van Der Zee, W., Schmatz, J., 2005. Shear zone formation and strain distribution in granular materials – new insights employing high-resolution optical image correlation. *Journal of Structural Geology* 27, 283–301.
- Antonellini, M.A., Aydin, A., Pollard, D.D., 1994. Microstructure of deformation bands in porous sandstones at Arches National Park, Utah. *Journal of Structural Geology* 16, 941–959.
- Barnhoorn, A., Bystricky, M., Burlini, L., Kunze, K., 2004. The role of recrystallisation on the deformation behaviour of calcite rocks: large strain torsion experiments on Carrara marble. *Journal of Structural Geology* 26, 885–903.
- Byerlee, J., 1978. Friction of rocks. *Pure and Applied Geophysics* 116, 615–626.
- Chu, J., 1995. An experimental examination of the critical state and other similar concepts for granular soils. *Canadian Geotechnical Journal* 32, 1065–1075.
- Cobbold, P.R., Castro, L., 1999. Fluid pressure and effective stress in sandbox models. *Tectonophysics* 301, 1–19.
- Colletta, B., Letouzey, J., Pinedo, R., Ballard, J.F., Bale, P., 1991. Computerized X-ray tomography analysis of sandbox models: examples of thinned thrust systems. *Geology* 19, 1063–1067.

- Desrues, J., 2004. Tracking strain localization in geomaterials using computerized tomography. In: Obara, Y., Otani, J. (Eds.), *X-ray CT for Geomaterials: Soils, Concrete, Rocks: International Workshop on X-ray CT for GeoMaterials*. A.A. Balkema Publishers, Rotterdam, pp. 15–41.
- Desrues, J., Viggiani, G., 2004. Strain localization in sand: an overview of the experimental results obtain in Grenoble using stereophotogrammetry. *International Journal for Numerical and Analytical Methods in Geomechanics* 28, 279–321.
- Ellis, S., Schreurs, G., Panien, M., 2004. Comparisons between analogue and numerical models of thrust wedge development. *Journal of Structural Geology* 26, 1659–1675.
- Hartmann, C., Poss, R., Janeau, J.L., Bourdon, E., Lesturgez, G., Ratana Anupap, S., 2002. Use of the Granular Material Theory to Interpret Structural Changes in a Sandy Soil. 17th WCSS Conference. Thailand, 2108.1–2108.11.
- Herrmann, H.J., 2001. Structures in deformed granular packings. *Granular Matter* 3, 15–18.
- Hubbert, M.K., 1937. Theory of scale models as applied to the study of geologic structures. *Geological Society of America Bulletin* 48, 1459–1520.
- Hubbert, M.K., 1951. Mechanical basis for certain familiar geologic structures. *Geological Society of America Bulletin* 62, 355–372.
- Jaeger, J.C., Cook, N.G.W., 1979. *Fundamentals of Rock Mechanics*. Chapman & Hall., London.
- Jaeger, H.M., Nagel, S., Behringer, R.P., 1996. Granular solids, liquids and gases. *Reviews of Modern Physics* 68, 1259–1273.
- Krantz, R.W., 1991a. Normal fault geometry and fault reactivation in tectonic inversion experiments. In: Roberts, A.M., Yielding, G., Freeman, B. (Eds.), *The Geometry of Normal Faults*, 56. Geological Society, London, pp. 219–229. Special Publications.
- Krantz, R.W., 1991b. Measurements of friction coefficients and cohesion for faulting and fault reactivation in laboratory models using sand and sand mixtures. *Tectonophysics* 188, 203–207.
- Kruyt, N.P., Rothenburg, L., 2004. Kinematic and static assumptions for homogenization in micromechanics of granular materials. *Mechanics of Materials* 36, 1157–1173.
- Lätzel, M., 2003. *From Microscopic Simulations Towards a Macroscopic Description of Granular Media*. PhD Thesis. University of Stuttgart. 172 p.
- Lohrmann, J., Kukowski, N., Adam, J., Oncken, O., 2003. The impact of analogue material properties on the geometry, kinematics and dynamics of convergent sand wedges. *Journal of Structural Geology* 25, 1691–1711.
- Mair, K., Frye, K.M., Marone, C., 2002. Influence of grain characteristics on the friction of granular shear zones. *Journal of Geophysical Research* 107 (B10), 4/1–4/9.
- Mandl, G., 1988. *Mechanics of Tectonic Faulting. Models and Basic Concepts*. Elsevier, Amsterdam.
- Marone, C., 1998. Laboratory-derived friction laws and their application to seismic faulting. *Annual Review of Earth and Planetary Sciences* 26, 643–696.
- Mandl, G., de Jong, L.N.J., Maltha, A., 1977. Shear zones in granular material. *Rock Mechanics* 9, 95–144.
- Mokni, M., 1992. *Relations entre déformations en masse et déformations localisées dans les matériaux granulaires*. PhD thesis. Université Joseph Fourier, Grenoble.
- Mueth, D.M., Jaeger, H.M., Nagel, S.R., 1998. Force distribution in a granular medium. *Physical Review E* 3, 3164–3169.
- Mühlhaus, H.B., Vardoulakis, I., 1987. The thickness of shear bands in granular materials. *Géotechnique* 37, 271–283.
- Nicolas, A., 1987. *Principles of Rock Deformation*. Reidel Publishing Company.
- Oda, M., Kazama, H., 1998. Microstructure of shear bands and its relation to the mechanisms of dilatancy and failure of dense granular soils. *Géotechnique* 48, 465–481.
- Panozzo, R.H., 1983. Two-dimensional analysis of shape-fabric using projections of digitized lines in a plane. *Tectonophysics* 95, 279–294.
- Panozzo, R., Hürlimann, H., 1983. A simple method for the quantitative discrimination of convex and convex-concave lines. *Microscopica Acta* 87, 169–176.
- Powers, M.C., 1953. A new roundness scale for sedimentary particles. *Journal of Sedimentary Petrology* 23, 117–119.
- Ramberg, H., 1981. The role of gravity in orogenic belts. In: McClay, K.R., Price, N.J. (Eds.), *Thrust and Nappe Tectonics; International Conference*, 9. Geological Society, London, pp. 125–140. Special Publications.
- Roscoe, 1970. The influence of strains in soil mechanics. *Géotechnique* 20 (2), 129–170.
- Rossi, D., Storti, F., 2003. New artificial granular materials for analogue laboratory experiments: aluminium and siliceous microspheres. *Journal of Structural Geology* 25, 1893–1899.
- Schanz, T., Vermeer, P.A., 1996. Angles of friction and dilatancy of sand. *Géotechnique* 46, 145–151.
- Schellart, W.P., 2000. Shear test results for cohesion and friction coefficients for different granular materials: scaling implications for their usage in analogue modelling. *Tectonophysics* 324, 1–16.
- Schreurs, G., Hänni, R., Vock, P., 2001. Four-dimensional analysis of analogue models: experiments on transfer zones in fold and thrust belts. In: Koyi, H.A., Mancktelow, N.S. (Eds.), *Tectonic Modelling: A Volume in Honor of Hans Ramberg, 193*. Geological Society of America Memoir, pp. 179–190.
- Schulze, D., 1994. Entwicklung und Anwendung eines neuartigen Ringschergärates. *Aufbereitungs-Technik* 35/10, 524–535.
- Vardoulakis, I., Graf, B., 1985. Calibration of constitutive models for granular materials using data from biaxial experiments. *Géotechnique* 35 (3), 299–317.
- Vardoulakis, I., Graf, B., Hettler, A., 1985. Shear-band formation in a fine-grained sand. *Proceedings 5th International Conference on Numerical Methods in Geomechanics*, Nagoya 1, A.A. Balkema Publishers, Rotterdam, pp. 517–521.
- Viggiani, G., Küntz, M., Desrues, J., 2001. An experimental investigation of the relationships between grain size distribution and shear banding in sand. In: Vermeer, P.A., Diebels, S., Ehlers, W., Hermann, H.J., Luding, S., Ramm, E. (Eds.), *Continuous and Discontinuous Modelling of Cohesive-Frictional Materials. Lecture Notes in Physics*, Springer, pp. 111–127.